🔓 Open Access Full Text Article

ORIGINAL RESEARCH

Self-Assembly Catalase Nanocomplex Conveyed by Bacterial Vesicles for Oxygenated Photodynamic Therapy and Tumor Immunotherapy

Jiayu Zhang[1,*], Zinan Li[2,*], Ling Liu[3], Longyun Li[2], Lu Zhang[2], Yongkun Wang[4], Jia Zhao[2]

[1]Department of Gastrointestinal Colorectal and Anal Surgery, China-Japan Union Hospital of Jilin University, Changchun, Jilin, People's Republic of China; [2]Department of Anesthesiology, China-Japan Union Hospital of Jilin University, Changchun, Jilin, People's Republic of China; [3]Department of Pediatrics, China-Japan Union Hospital of Jilin University, Changchun, Jilin, People's Republic of China; [4]Department of Orthopedic, China-Japan Union Hospital of Jilin University, Changchun, Jilin, People's Republic of China

*These authors contributed equally to this work

Correspondence: Jia Zhao, Department of Anesthesiology, China-Japan Union Hospital of Jilin University, Changchun, Jilin, People's Republic of China, Email zj5413@jlu.edu.cn; Yongkun Wang, Department of Orthopedic, China-Japan Union Hospital of Jilin University, Changchun, Jilin, People's Republic of China, Email wangykun@jlu.edu.cn

Background: Photodynamic therapy (PDT) is an effective therapeutic modality that has been extensively studied in treatment of various cancers. However, issues with inadequate oxygen (O_2) concentration in tumor tissue and inadequate immune response generation have hindered its successful application in tumor therapy.

Methods: Firstly, the self-assembly nanocomplex (CAT-Ce6), which is composed of hydrophilic catalase and hydrophobic photosensitizer Chlorin e6 (Ce6), was fabricated to support oxygenated PDT. Secondly, for supplying PDT with enhanced antitumoral immunity, CAT-Ce6 was coated with PD-L1 antibody modified-attenuated *Salmonella* outer membrane vesicles (OMV-aPDL1). Finally, the catalytic activity, tumor targeting, hypoxia ameliorating, immune effect initiating and anti-tumor capacities of the integral nanosystem CAT-Ce6@OMV-aPDL1 were evaluated systematically.

Results: The self-assembly nanocomplex (CAT-Ce6) generated sufficient O_2 and promoted the solubility of Ce6 simultaneously, which enhanced PDT significantly. OMV-aPDL1 inherited most of the immunogenic membrane-associated components from the parent bacteria, possessing immunomodulation ability for immunosuppressive tumor microenvironment reprograming and reducing immune escape. The obtained nanosystem CAT-Ce6@OMV-aPDL1 durably relieved hypoxia, resulting in amplifying PDT-mediated cytotoxicity to generate a pool of tumor-associated antigens, stimulating anti-tumor immune responses and even inducing an immune memory effect, which inhibited tumor development efficiently.

Conclusion: The resultant CAT-Ce6@OMV-aPDL1 displays excellent efficacy of PDT and immunotherapy to achieve antitumor effects, which provides a new avenue for combinatorial therapy against various cancers.

Keywords: oxygenated photodynamic therapy, anti-tumor immune response, long term hypoxia relieving, immune memory effect

Introduction

Photodynamic therapy (PDT), which induces chemical damage and death of tumor cells by generating reactive oxygen species (ROS) such as singlet oxygen ($^1O_2$) through local activation of a photosensitizer (PS) under laser irradiation, has been widely used in various malignant tumors therapy.[1–4] PDT has several advantages over chemotherapy and radiotherapy including invasiveness, low side effects and great spatiotemporal selectivity, but the high O_2 dependence of PDT leads to its limited therapeutic effect on hypoxic solid tumors.[5–9]

To address this obstacle, efforts have been made to elevate the amount of O_2 in the targeted tumor thereby enhancing the PDT efficacy, including conveying exogenous O_2 to tumor, producing O_2 in situ, regulating tumor microenvironments, regenerating $^1O_2$ depending on structural changes of chemical substance and so on.[10–14] The negatively charged catalase (CAT), which is characteristic of self-responsivity to hydrogen peroxide (H_2O_2), is a promising O_2 supplement agent.[15,16] It can continuously increase the yield of dissolved O_2 by catalyzing H_2O_2 in tumor tissues and improve the tumor hypoxic environment.[17–19] PS is another decisive factor relating to PDT activity, which should satisfy some desirable properties such as low dark toxicity, high extinction coefficients, and proper water solubility.[20,21] Jiang et al. designed an amphiphilic boron dipyrromethene (BODIPY) derivative with tunable water solubility, good PDT activity and low cell toxicity for new vessels treatment.[22] Chlorin e6 (Ce6) is one of the well-serviceable PSs with high $^1O_2$ yield in PDT treatment.[23–26] However, the easy aggregation in aqueous solution, weak tumor tendency and rapid blood clearance are the main defects hindering its application.[27,28] Nevertheless, we found that catalase and Ce6 can self assemble to form an amphiphilic complex, which ultimately not only enhances the therapeutic effect of PDT by supplementing the O_2 content of the tumor microenvironment, but also improves the dispersion and compatibility of Ce6 under physiological conditions, thus magnifying the tumor killing effect.

To optimize the therapeutic outcome of PDT, we tried to combine oxygenated PDT with immunotherapy. However, insufficient immune arousal and tumor immune escape limited the efficacy of immunotherapy.[29–31] The discovery of treatments with the capacity of tumor targeted aggregation, efficient immune stimulation and comprehensive immune penetration in tumor microenvironment will always be the focus of researchers.[32,33] The nanosized bacterial outer membrane vesicles (OMVs) containing endogenous immune-stimulating components such as lipopolysaccharide (LPS), outer membrane proteins and lipoproteins have the ability to regulate tumor immunosuppressive microenvironment and passively accumulate in tumors.[34–38] Programmed death-ligand 1 antibody (aPDL1) is proved to relieve the immuno-suppressive effect, activate T lymphocytes, and enhance immune surveillance against tumors based on immune checkpoint inhibitor treatment (ICB).[39,40] Therefore, modification of OMVs with aPDL1 can simultaneously eliminate tumor immune escape while stimulating the immune response, and help lymphocytes to infiltrate and kill tumors.[41–43]

In this work, we developed a combinatorial anti-tumor approach based on oxygenated PDT and immunotherapy (Scheme 1). The PS Ce6 was uploaded to the molecular scaffold in combination with catalase (CAT-Ce6), which ameliorated tumor hypoxia, improved the aggregation of free Ce6, enhanced photodynamic killing effect and tumor associated antigen exposure to evoke immune response. Nanosized attenuated *Salmonella* OMVs with aPDL1 modified (OMV-aPDL1) were utilized to convey CAT-Ce6 with synergic stimulating anti-tumor immunity and increasing lymphocyte infiltration, which further cleaning the tumor microenvironment, so as to achieve the purpose of inhibiting tumor expansion. In view of the availability and biosafety of materials, our combined therapy system owns broad potential for clinical application.

Materials and Methods
Materials

Catalase and Ce6 were purchased from Solarbio (Beijing, China). PD-L1 antibody (aPDL1) was purchased from Cell Signaling Technology (USA). 1-Ethyl-3-(3-(dimethylamino) propyl) carbodiimide (EDC) and n-hydroxysuccinimide (NHS) were purchased from Sigma (USA). Antibody against mouse H-2K^b bound to SIINFEKL was purchased from Biolegend (San Diego, CA, USA). Other antibodies (CD11c, CD80, CD86, CD3, CD8, CD44, CD62L) were purchased from Proteintech (Rosemont, IL, USA).

Cell Cultures and Bacteria Culture

Mouse mammary carcinoma cell line 4T1 was purchased from American Type Culture Collection (ATCC, Shanghai). Cells were cultured in Dulbecco's modified Eagle medium (DMEM) containing 10% fetal bovine serum (FBS), 100 IU mL^{-1} of penicillin at 37 °C in 5% CO_2.

Attenuated *Salmonella* was purchased from American Type Culture Collection (ATCC, Rockville, MD, USA) and cultured on Luria broth (LB) medium.
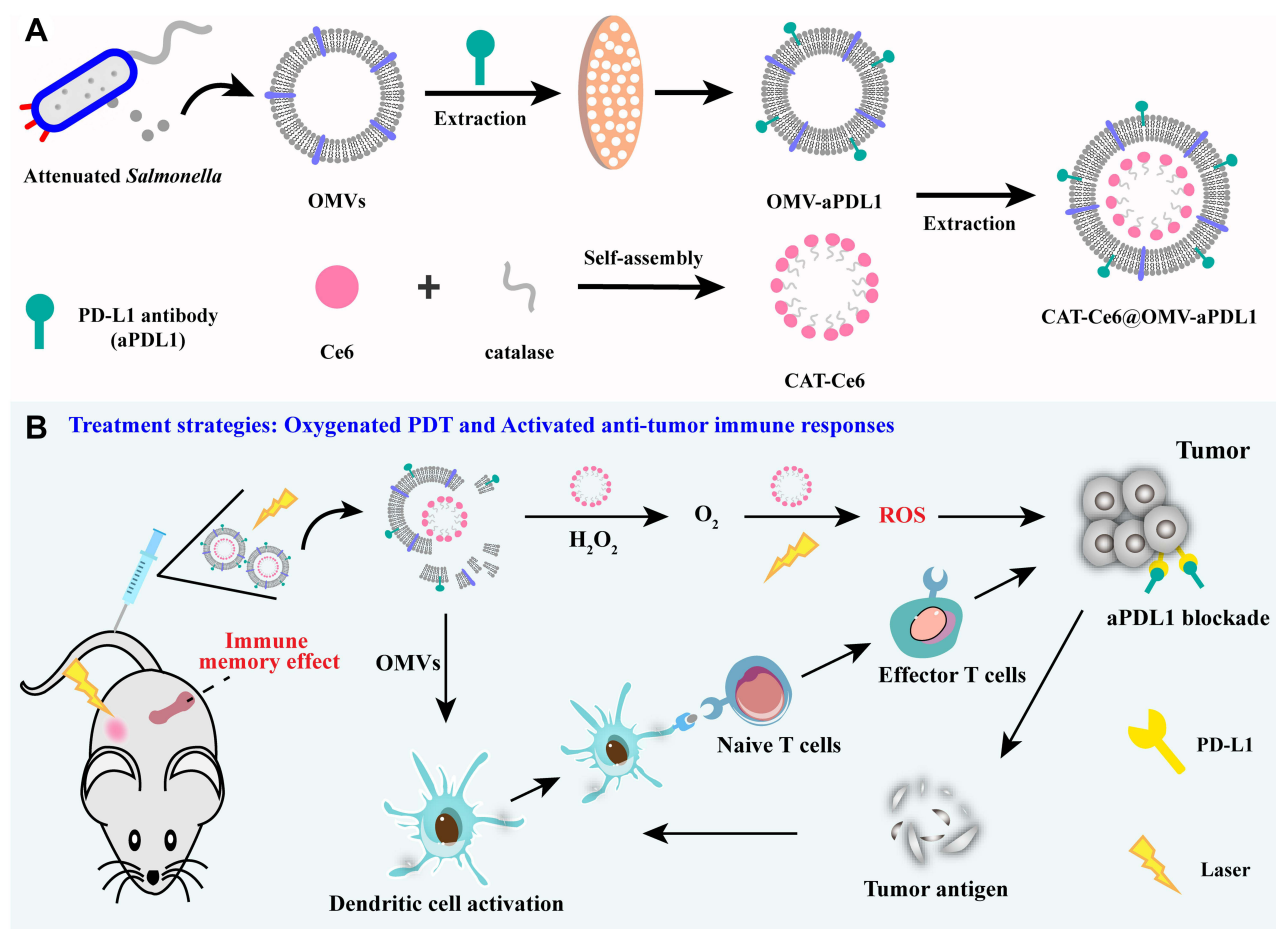
Scheme I Construction of CAT-Ce6@OMV-aPDL1 (**A**) and illustrations of promoted oxygenated PDT as well as activated anti-tumor immune responses induced by CAT-Ce6@OMV-aPDL1-based PDT and immunomodulation (**B**).

Synthesis of CAT-Ce6

The synthesis of CAT-Ce6 followed the previous method.[44] In brief, 0.64 mg EDC and 0.42 mg NHS were mixed with Ce6 (0.5 mL, 20 mg mL^{-1}) DMSO solution under stirring in the dark (room temperature) for 0.5 h. Thereafter, 5 mL catalase solution (1 mg mL^{-1}) dissolved in phosphate buffer saline (PBS) was added in the mixture from the previous step. The new liquid was stirred overnight in the dark under room temperature to harvest the crude product. Then, the crude product was subjected to dialysis in 500 mL PBS solution for 2 h to discard free Ce6, catalase, EDC and NHS.

Isolation and Purification of OMVs

OMVs were isolated from bacterial culture medium by gradient centrifugation. When bacteria were in logarithmic growth period, 250 mL culture medium was centrifuged at 4000 g for 15 min to remove *Salmonella* and then the supernatant was filtered through 0.45 μm pore size filters. Afterwards, the filtrate was concentrated by centrifugal filters (100 kDa, Millipore, USA). The product was further concentrated by ultracentrifugation (L-80XP, Beckman, USA) at 150,000 g for 2 h at 4 °C. For purification, the product was resuspended in PBS solution and layered over a sucrose gradient, followed by separation at 45000 rpm at 4 °C for 1 h. Finally, OMVs were stored at −80 °C for further experiments.

Synthesis and Characterization of CAT-Ce6@OMV-aPDL1

PD-L1 antibody modified OMVs (OMV-aPDL1) was formed by extrusion. In brief, 0.5 mL aPDL1 (10μg mL^{-1}) was blended with 0.5 mL OMV PBS solution (500 μg mL^{-1}) and co-extruded through 200 nm polycarbonate films 10 times.

After that, CAT-Ce6 was added in the OMV-aPDL1 (1:1, v/v) for co-extrusion (x 20 times) through 200 nm poly-carbonate films to harvest CAT-Ce6@OMV-aPDL1.

The morphologies, average sizes and zeta potentials of CAT-Ce6, OMVs and CAT-Ce6@OMV-aPDL1 were analyzed using TEM (JEM-2000 EX II, JEOL Company, USA) and DLS (Litesizer 500, Anton Paar, Austria) respectively. SDS–polyacrylamide gel electrophoresis (SDS-PAGE) was used to detect the uploading of different constituents. Each sample was blended with loading buffer (New Cell & Molecular, Suzhou, China) and the protein mixture was denatured by boiling for 10 min. Then, all samples were separated on Bis-Tris gel (Beyotime, Shanghai, China) for about 2 h. Afterwards, the gel was cut and stained for further analysis.

The Encapsulation Efficiency and Loading Rate of CAT-Ce6

A series of CAT-Ce6@OMV-aPDL1 solutions with increasing concentration of CAT-Ce6 were synthesized. After purification, CAT-Ce6@OMV-aPDL1 solutions were cooled at $-80°C$ for 30 min and then lyophilized overnight, followed by demulsification. The concentration of CAT-Ce6 complex was measured by fluorospectrophotometer (Spectrofluorometer FS5, Edinburgh Instruments, UK).

The Drug Release of CAT-Ce6@OMV-aPDL1

Drug release study of CAT-Ce6@OMV-aPDL1 was investigated using dialysis method. In brief, 2 mL CAT-Ce6@OMV-aPDL1 solution was packed in dialysis bags (MWCO, 3.5 kDa) and merged into 100 mL PBS solution. Then, the experiment was carried out with or without laser irradiation ($0.15 W/cm^2$, 10 min). At predetermined time points, 1 mL dissolution media was taken out for measuring the drug release rate using a fluorospectrophotometer.

Evaluation of the Catalase Activity and Stability Against Protease K of CAT-Ce6

First, CAT-Ce6 was incubated with H_2O_2 solution to evaluate the enzymatic activity of catalase. In brief, the reaction solution ($0.5 mM H_2O_2$) was removed of dissolved O_2 via filling with nitrogen in advance. Then free catalase or CAT-Ce6 (with same catalase concentration) was added into the solution to react for 200 s. PBS solution was served as control group. A probe of dissolved O_2 meter was used to record the concentration of dissolved O_2.

Then, free catalase or CAT-Ce6 (with same catalase concentration) was incubated with protease K ($0.4 mg mL^{-1}$) at 37 °C. At predetermined time points, reaction solution was collected for catalase activity assay the same as described above.

Extracellular Measurement of O_2 Concentration

CAT-Ce6, Ce6@OMV, CAT-Ce6@OMV-aPDL1 were added in the reaction solution ($1mM H_2O_2$) respectively, which was removed of dissolved O_2 in advance. PBS solution served as the control group. Afterwards, a probe of dissolved O_2 meter was used to record the concentration of dissolved O_2 during 15 min.

Extracellular Measurement of $^1O_2$ Concentration

The 1,3-diphenylisobenzonfuran (DPBF, Sigma-Aldrich) probe was used to detect the $^1O_2$ generation as previously reported.[45] In brief, 2 mL reaction mixture (1 mM H_2O_2 and nanoparticle solution) was mixed with DPBF solution (10 μL, 10 mM in DMSO) under laser irradiation (660 nm, $0.15 W/cm^2$) for 10 min. The absorbance of DPBF at 420 nm was recorded every minute to measure the concentration of $^1O_2$.

In vivo Fluorescence Imaging

6-weeks old Balb/c mice were purchased from Qinglongshan Animal Breeding Farm (Nanjing, China). All animal studies complied with the China National Institute's Guidelines on the Care and Use of Laboratory Animals and were performed according to National Institute of Health (NIH) Guide and approved by the Laboratory Animal Management Committee of Jilin University. Subcutaneous 4T1 tumor-bearing mice were intravenously injected with 100 μL free Ce6, CAT-Ce6 or CAT-Ce6@OMV-aPDL1. At predetermined time points, mice were exposed to IVIS Lumina System (IVIS Lumina XR, USA) to detect the distributions of different formulations. At 24 h post-injection, mice were dissected and tumor, heart, liver, spleen, lung, kidney were collected for ex vivo fluorescence imaging. Tumor tissues were sectioned

and stained for detecting the tumor infiltration of different formulations using confocal laser scanning microscopy (CLSM) (LSM800, Zeiss, Germany).

Long-Term Alleviating Hypoxia of CAT-Ce6@OMV-aPDL1

Subcutaneous 4T1-tumor bearing mice were intravenously injected with CAT-Ce6 and CAT-Ce6@OMV-aPDL1 respectively. PBS was served as control. 8 h later, mice were exposed to 660 nm laser irradiation (0.15 W/cm^2) for 10 min. 12 and 24 h after light illumination, tumors were dissected and embedded with an optimal cutting temperature compound (OCT) for making frozen sections. Then sections were stained against HIF-1α and DAPI for observing the degree of alleviating hypoxia.

In vitro Cell Cytotoxicity of CAT-Ce6@OMV-aPDL1 Inducing by PDT

Cellular toxicity was assessed by MTT test. 5×10^3 4T1 cells were seeded into a 96-well plate per well and cultured overnight. Then different formulations with increasing concentrations of Ce6 were added into the wells (n = 6). 2 h later, cells were exposed to laser irradiation (660 nm, 0.15 W/cm^2, 5 min) or not. 12 h later, 15 μL MTT (BioFroxx, Guangzhou, China) solution (5.0 mg mL^{-1} PBS) was added into each well and incubated with cells for 4 h. Finally, the mixture solution in each well was poured out and replaced by 150 μL DMSO for determining the cell toxicity using microplate reader under 520 nm.

Cell Apoptosis Assay

3×10^5 4T1 cells were seeded into a 6-well plate. The next day, cells were incubated with PBS, CAT-Ce6, Ce6@OMV, CAT-Ce6@OMV and CAT-Ce6@OMV-aPDL1 (Ce6 concentration: 8 μg mL^{-1}), followed by laser irradiation (660 nm, 0.15 W/cm^2, 5 min) 2 h later. 12 h later, cells were digested and stained following the instruction of Annexin V-FITC/PI apoptosis detection kit (KeyGen, Nanjing, China) for measuring the cell apoptosis and necrosis rate using flow cytometry (FCM, BD, America).

Intracellular ROS Detection

3×10^4 4T1 cells were seeded into a confocal dish under hypoxic conditions. The next day, cells were incubated with different formulations, followed by adding of cell-permeant 2',7'-dichlorodihydrofluorescein diacetate (H2-DCFDA, 25 μM) and subjecting to laser irradiation as described above. 4 h later, cells were rinsed with PBS and stained with DAPI to observe the ROS generation using CLSM.

In vitro Evaluation of BMDCs Activation Effect

Bone marrow derived dendritic cells (BMDCs) were collected from marrow cavities of femurs and tibias of mice and seeded into a 6-well plate. The next day, BMDCs were treated with PBS, CAT-Ce6, Ce6@OMV, CAT-Ce6@OMV and CAT-Ce6@OMV-aPDL1 respectively. After 24 h incubation, cell suspensions were rinsed with PBS and stained with SINFEKL/H-2K^b antibody for detecting the degree of function-activated DCs using FCM.

Anti-Tumor Effect Experiment

6-weeks old Balb/c mice were subcutaneously inoculated with 4T1 cells (5×10^6) and divided randomly into 5 groups (n = 5) when the tumor reached 80 mm^3. Then, mice were intravenously injected via tail vein with 100 μL PBS, CAT-Ce6, Ce6@OMV, CAT-Ce6@OMV, or CAT-Ce6@OMV-aPDL1 (Ce6 concentration: 8 μg mL^{-1}), followed by laser irradiation (660 nm, 0.15 W/cm^2, 10 min) 8 h later. Treatments were carried out on days 7 and 14. And body weights as well as tumor volumes of mice were measured every 3 days to assess the anti-tumor efficacy. On day 22, mice were dissected and tumors were collected for immune fluorescence staining against TUNEL and H&E staining.

In vivo Evaluation of Immune Activation Effect

4T1-tumor bearing mice were treated with PBS, CAT-Ce6, Ce6@OMV, CAT-Ce6@OMV, and CAT-Ce6@OMV-aPDL1 (Ce6 concentration: 8 μg mL^{-1}), followed by laser irradiation (660 nm, 0.15 W/cm^2, 10 min) 8 h later. 5 days after

the second treatment, tumor tissues were collected and digested for preparing single cell suspensions. Then cell suspensions were stained against CD11c, CD80, CD86 antibodies for detecting the degree of mature dendritic cells (DCs).

At the same time, tumor tissues were embedded with OCT for making frozen sections and stained against with CD3, CD8 antibodies to detect the tumor infiltration of CD8$^+$ T cell.

Quantification of Cytokines in the Serum and Tumor Tissue

4T1-tumor bearing mice were injected with PBS, CAT-Ce6, Ce6@OMV, CAT-Ce6@OMV, and CAT-Ce6@OMV-aPDL1 (Ce6 concentration: 8 μg mL^{-1}), followed by laser irradiation (660 nm, 0.15 W/cm^2, 10 min) 8 h later. At predetermined time points post treatment, mice were killed and blood was collected for serum cytokines evaluation. Meanwhile, tumor tissues were digested for preparing single cell suspensions, followed by centrifuging at 1500 g for 20 min at 4 °C to retain the supernatant. The cytokines (IFN-γ, TNF-α, and IL-12p40) evaluation was carried out by Elisa following the manufacturer's instructions.

Effector Memory T Cell Assay

4T1-tumor bearing mice were treated with PBS, CAT-Ce6, Ce6@OMV, CAT-Ce6@OMV, and CAT-Ce6@OMV-aPDL1 (Ce6 concentration: 8 μg mL^{-1}), followed by laser irradiation (0.15 W/cm^2, 10 min) 8 h later. 7 days after the last treatment, spleen tissues were collected and digested for preparing single cell suspensions. Then cell suspensions were stained against CD3, CD8, CD44, CD62L antibodies for detecting the proportion of effector memory CD8$^+$ T cells using FCM.

Statistical Analysis

Data are presented as mean ± standard deviation (mean ± SD) and analyzed using GraphPad Prism software. Student's t-test was used to compare the difference between two groups, a one-way analysis of variance (ANOVA) was used to compare the difference between multiple groups and log-rank (Mantel–Cox) test was used to assess survival rate. The value of $p < 0.05$ was considered statistically significant.

Results

Characterization of CAT-Ce6@OMV-aPDL1

At first, Ce6 was conjugated covalently with catalase through sample synthesis routes. Then, CAT-Ce6@OMV-aPDL1 was harvested via co-extrusion between CAT-Ce6 and OMV-aPDL1. TEM images demonstrated that CAT-Ce6 was a very good approximation to a sphere with a uniform size distribution, OMVs exhibited a concave hemisphere-like structure, and CAT-Ce6@OMV-aPDL1 showed a homogeneous spherical-like morphology with bilayer membrane structure (Figure 1A). The results of DLS accurately measured that CAT-Ce6@OMV-aPDL1 was slightly larger with a hydrodynamic diameter of 140.907 nm and a slightly rising zeta potential of −19 mV relative to OMVs, which indicated the successful synthesis of CAT-Ce6@OMV-aPDL1 (Figure 1B). For further verifying the successful uploading of each composition, SDS-PAGE was used for component analysis at the protein aspect. As Figure 1C revealed, CAT-Ce6@OMV-aPDL1 not only had similar protein bands to OMVs but also characteristic bands of catalase and aPD-L1, which confirmed the success of its construction. The final encapsulation efficiency and loading rate of CAT-Ce6 were 51.4% and 31.85% (Figure 1D and E).

The successful synthesis of CAT-Ce6@OMV-aPDL1 was examined by the above experiments, and a series of features such as stability and enzymatic activity were next investigated. As depicted in Figure 1F, CAT-Ce6@OMV-aPDL1 was stable in PBS and FBS (25 °C) solution for up to 7 days while its size remained 140~145 nm. The CAT-Ce6 release rate of CAT-Ce6@OMV-aPDL1 is light-triggered as evidenced by the drug release profile in vitro. When laser was irradiated, the release rate rose rapidly to near 80% within 10 minutes compared to slight release without laser (Figure 1G). The decomposition of H$_2$O$_2$ by CAT-Ce6 remained almost identical to that of catalase, indicating that the synthesis of CAT-Ce6 did not disturb the active center of catalase (Figure 1H). Then the enzymatic activity of CAT-Ce6 and catalase after
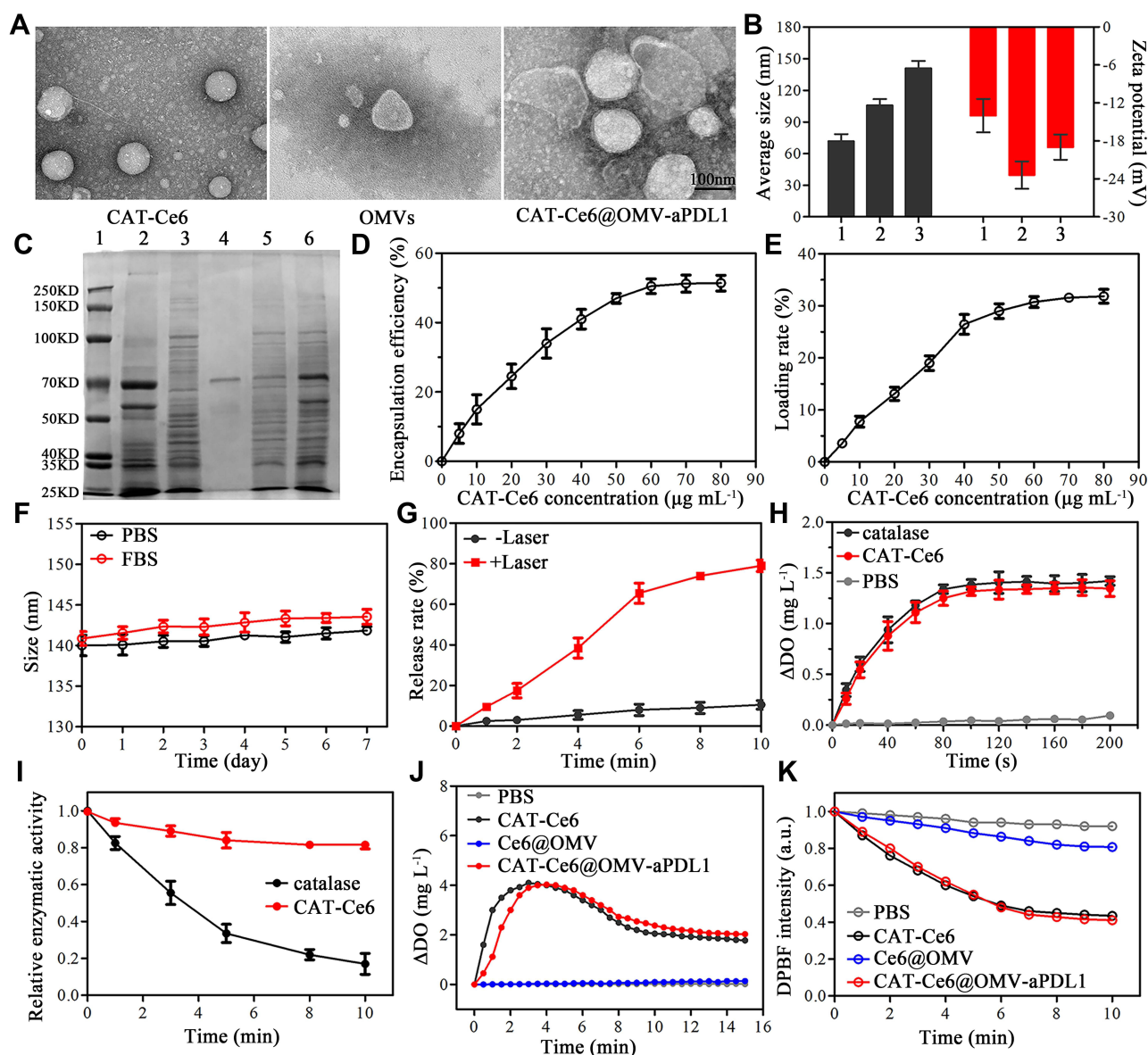
Figure 1 Characterization of CAT-Ce6@OMV-aPDL1. (**A**) The TEM images of CAT-Ce6, OMVs, CAT-Ce6@OMV-aPDL1. Scale bar, 100 nm. (**B**) Average sizes and zeta potentials of different agents: (1) CAT-Ce6, (2) OMVs, (3) CAT-Ce6@OMV-aPDL1. (**C**) Protein patterns of different agents: (1) marker, (2) catalase, (3) OMVs, (4) aPD-L1, (5) OMV-aPDL1, (6) CAT-Ce6@OMV-aPDL1. Encapsulation efficiency (**D**) and loading rate (**E**) of CAT-Ce6. (**F**) The stability of CAT-Ce6@OMV-aPDL1 in PBS and FBS (25 °C) solution during 7 days. (**G**) The release rate of CAT-Ce6 under laser irradiation or not. (**H**) The catalytic activity of catalase in CAT-Ce6. (**I**) The catalytic activity of catalase or CAT-Ce6, which was pretreated with protease K (0.4 mg mL^{-1}) at different times. (**J**) O$_2$ concentration of different formulations after incubating with H$_2$O$_2$ solution (H$_2$O$_2$= 1mM). (**K**) Time-dependent degradation of DPBF after incubating with different formulations under laser irradiation.

protease K digestion at different times was tested in Figure 1I, which revealed that CAT-Ce6 had a much higher stability against enzymatic hydrolysis, maintaining decomposing H$_2$O$_2$ efficiently. Furthermore, different formulations were incubated with H$_2$O$_2$ solution to testify their capacity of decomposing H$_2$O$_2$ to produce O$_2$. Compared with poor O$_2$ generation of Ce6@OMV, CAT-Ce6@OMV-aPDL1 group produced much more O$_2$ equivalent to CAT-Ce6 group (Figure 1J). In parallel, the ^{1}O$_2$ generation of CAT-Ce6@OMV-aPDL1 in vitro was monitored utilizing DPBF as the chemical probe. The DPBF content of CAT-Ce6@OMV-aPDL1 group showed a remarkable decrease compared with Ce6@OMV group under the laser, indicating a pronounced ^{1}O$_2$ generation (Figure 1K). These results corroborated that CAT-Ce6@OMV-aPDL1 maintained the catalytic activity of catalase as well as elevating its resistance against protease hydrolysis, which had the potential to catalyze H$_2$O$_2$ in vitro and vivo to produce enough O$_2$ to promote the therapeutic effect of PDT.

In vivo Biodistribution and the Long-Time Hypoxia Relief of CAT-Ce6@OMV-aPDL1

Prior to exploring the tumor targeting capability of CAT-Ce6@OMV-aPDL1 in vivo, we assessed the cellular uptake of different formulations (Ce6, CAT-Ce6, CAT-Ce6@OMV-aPDL1) after incubation with 4T1 cells. As shown in Figure S1, significantly stronger fluorescence signal was observed in CAT-Ce6 and CAT-Ce6@OMV-aPDL1 groups. And it was worth noting that more CAT-Ce6@OMV-aPDL1 was internalized by 4T1 cells compared with CAT-Ce6, which might be attributed to some functional proteins carried by OMVs. Afterwards, we studied the in vivo biodistribution behaviors of CAT-Ce6@OMV-aPDL1 at different times. Free Ce6, CAT-Ce6, and CAT-Ce6@OMV-aPDL1 were individually injected into 4T1 tumor-bearing mice. The fluorescence signal at the tumor site was monitored by an optical imaging system for living small animals. Over time, CAT-Ce6 and CAT-Ce6@OMV-aPDL1 were accumulated at tumor sites to a large extent because of passive targeting compared with free Ce6 group, while the latter was stronger and the fluorescence intensity of CAT-Ce6 @OMV-aPDL1 group increased steadily until reaching a peak at 8 h (Figure 2A). This difference might be ascribed to the enhanced permeability and retention effect (EPR) of OMVs. The ratio of drug fluorescence signal between tumor and normal tissue (T/NT) also confirmed the most drug retention in tumor of CAT-Ce6@OMV-aPDL1 group (Figure S2A). Moreover, drug fluorescence signal in blood over time implied that Ce6@OMV-aPDL1 featured a longer circulation time, which favors drug accumulation in tumor as well (Figure S2B). At 24 h post-injection, the ex vivo images of tumor and organs further validated the long-term retention of CAT-Ce6@OMV-aPDL1 in the liver and more importantly in the tumor, compared with the free Ce6 group (Figure 2B). A similar conclusion was also attested by the immunofluorescence staining of tumor sections when observing the tumor infiltration of different formulations (Figure 2C).

The efficiency of tumor oxygenation with CAT-Ce6@OMV-aPDL1 was further investigated by HIF-1α probe immunofluorescence assay. 4T1-tumor bearing mice were injected with CAT-Ce6 and CAT-Ce6@OMV-aPDL1 respectively, followed by laser irradiation 8 h later. As Figure 2D revealed, 12 h after the laser irradiation, both CAT-Ce6 and CAT-Ce6@OMV-aPDL1 induced decreased HIF-1α expression to some extent. However, at 24 h post laser irradiation, the hypoxia area was barely detectable in the tumor section of the CAT-Ce6@OMV-aPDL1 group compared with CAT-Ce6 group, which might be due to enhanced tumor accumulation and higher stability of CAT-Ce6@OMV-aPDL1 against complex physiological conditions. It revealed that the tumor hypoxia was drastically attenuated by the O_2 supplement of CAT-Ce6@OMV-aPDL1 with long-lasting oxygenation capability. For studying the systemic toxicity of CAT-Ce6 @OMV-aPDL1, healthy mice were injected with CAT-Ce6@OMV-aPDL1 twice and the major organs were harvested for histological analysis 7 days after the last injection. No major organ damage was observed compared with PBS group, indicating good biocompatibility and biosafety of CAT-Ce6@OMV-aPDL1 (Figure 2E). All in all, CAT-Ce6@OMV-aPDL1 displayed a great ability to accumulate in and reduce hypoxia of tumor tissue for a long duration to ensure effective antitumor PDT.

In vitro Cell Cytotoxicity and Immune Activation Assays

MTT was used to evaluate the toxicity of different formulations to 4T1 cells before and after laser irradiation. Cell viability of 4T1 cells after each treatment was over 80% without laser irradiation, which indicated the safety of different formulations (Figure 3A). However, once laser added, all formulations presented cytotoxicity in a dose-dependent manner (Figure 3B). CAT-Ce6@OMV-aPDL1+L, CAT-Ce6@OMV+L and CAT-Ce6+L showed the similar cytotoxicity among all formulations. Also, cell survival rate of CAT-Ce6@OMV-aPDL1+L decreased to about 30% when Ce6 was applied at 8 μg mL^{-1}, proving an excellent photoresponse performance of the vector and a powerful lethality of the nanosystem based on PDT. FCM was further employed to detect the rate of dead 4T1 cells after incubation with different formulations, which was consistent with MTT results (Figure 3C). Subsequently, intracellular ROS generation was observed by CLSM with DFCH-DA as the probe (Figure 3D). Red fluorescence represented intracellular ROS production. After incubating with Ce6 in different forms and exposing to laser irradiation for 5 min, strong fluorescence intensity was observed in the CAT-Ce6+L, CAT-Ce6@OMV+L and CAT-Ce6@OMV-aPDL1+L groups. Therefore, the nanocomplex of CAT-Ce6 may cause a significant increase of dissolved O_2 content thus more ROS could be generated, which ultimately gives rise to larger population of dead tumor cells. In addition to killing effect on cancer cells of different formulations, stimulation on DCs was also elucidated by FCM. SINFEKL/H-2K^b complex is a peptide which can indicate the degree of antigen cross-presentation of DCs. As shown in
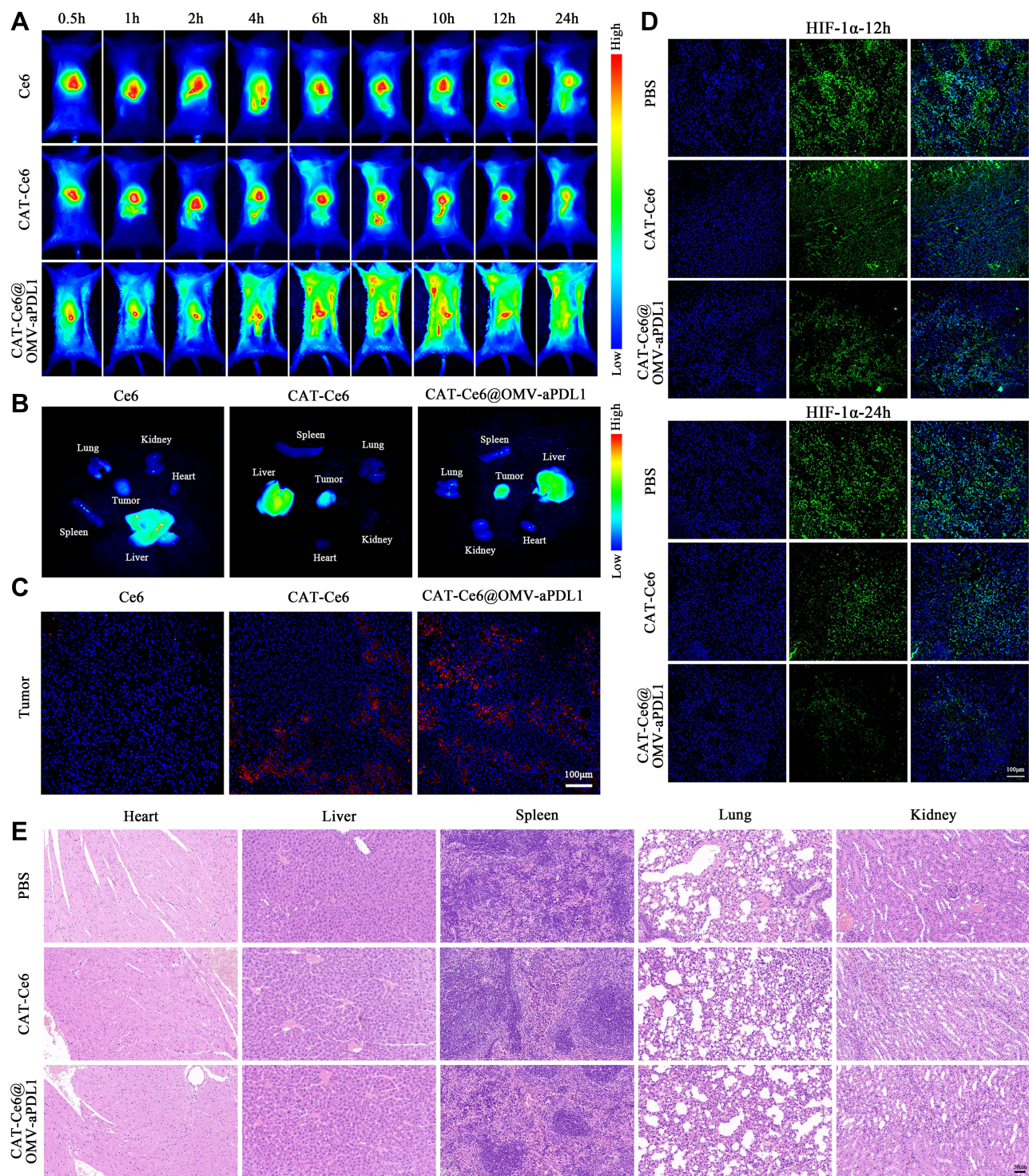
Figure 2 Biodistribution and long-term hypoxia relief of CAT-Ce6@OMV-aPDL1 in vivo. (**A**) The biodistribution of free Ce6, CAT-Ce6 and CAT-Ce6@OMV-aPDL1 over time. (**B**) Organs and tumor distribution of different formulations ex vivo at 24 h post-injection. (**C**) Tumor infiltration of different formulations at 24 h post-injection. Scale bar, 100 μm. (**D**) The hypoxia relief degree at 12, 24 h post laser irradiation of CAT-Ce6 or CAT-Ce6@OMV-aPDL1 group. Blue: DAPI, green: Alexa Fluor488-conjugated Hif-1α antibody. Scale bar, 100 μm. (**E**) Micrographs of five main organs measured by H&E staining after two intravenous injections of PBS, CAT-Ce6 or CAT-Ce6@OMV-aPDL1. Scale bar, 50 μm.

Figure 3E, comparing with low signal of SINFEKL/H-2K^b antibody in CAT-Ce6 group, the antigen cross-presentation by DCs was pronouncedly strengthened when OMVs were coated on the surface of CAT-Ce6, representing the function activation of DCs, which contributed from the natural immune activation capacity of OMVs. These results revealed that the OMVs shell
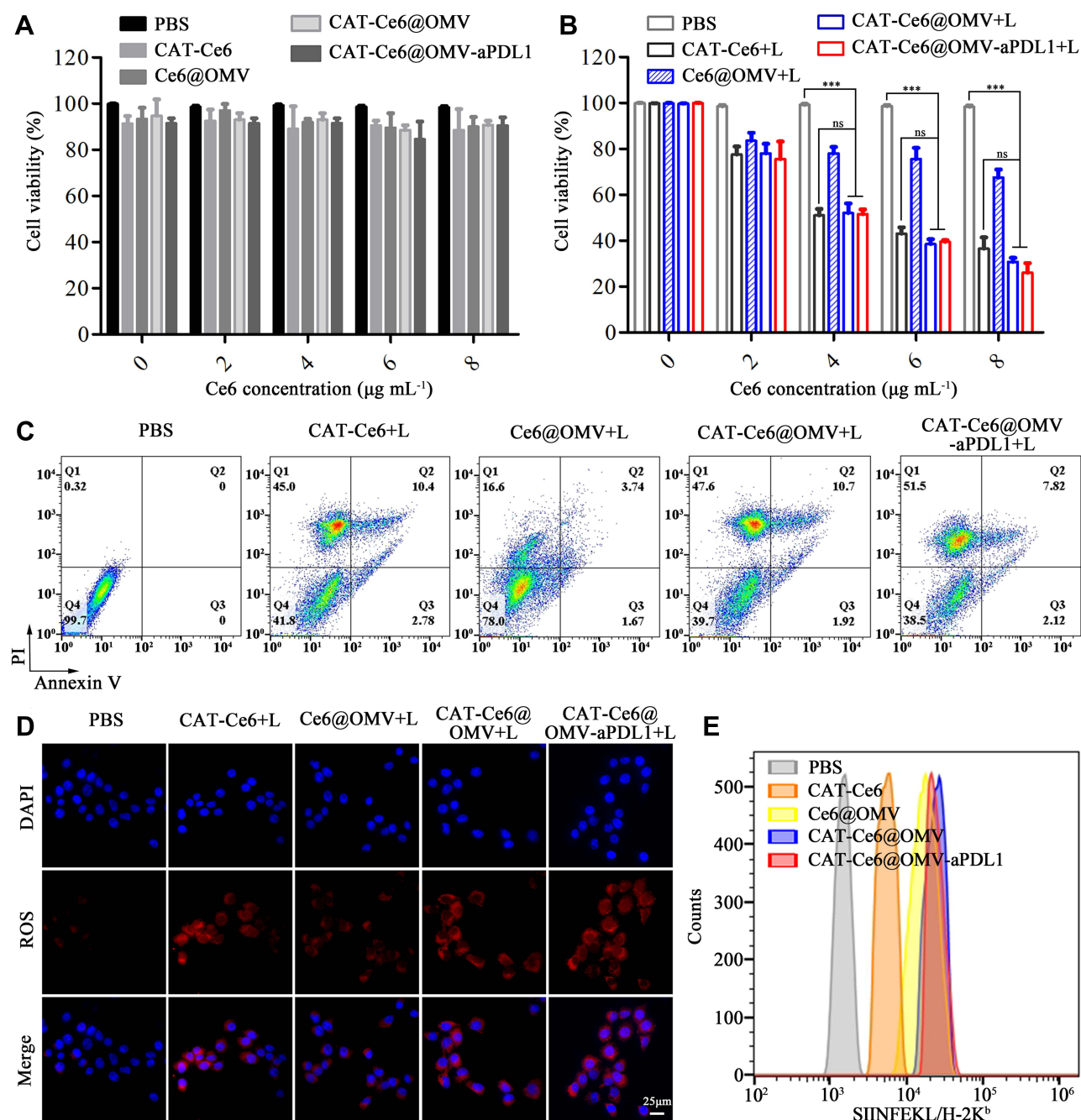
Figure 3 In vitro cell cytotoxicity and immune activation assay. Cell viability of 4T1 cells after incubated with PBS, CAT-Ce6, Ce6@OMV, CAT-Ce6@OMV, CAT-Ce6 @OMV-aPDL1 without (**A**) or with (**B**) laser irradiation (660 nm, 0.15 W/cm^2, 5 min). (**C**) Cell death rate of 4T1 cells after incubation with different formulations with laser irradiation. (**D**) ROS production of 4T1 cells after incubation with different formulations under laser irradiation. (**E**) Staining of SINFEKL/H-2K^b antibody to assess the surface presentation of antigen by DCs after incubated with different formulations. Data are presented as mean ± SD, statistical significance was analyzed by one-way ANOVA, ns = $P \geq 0.05$, ***$P < 0.001$.

could induce DCs activation significantly, which may contribute to enhanced tumor mortality coordination with CAT-Ce6 based PDT in vivo.

In vivo Treatment Efficiency of CAT-Ce6@OMV-aPDL1 Under Laser Irradiation

The treatment efficiency of CAT-Ce6@OMV-aPDL1 uniting with laser irradiation in vivo was investigated in the subcutaneous 4T1-tumor bearing model. The treatment round was carried out as described in Figure 4A. Body weights
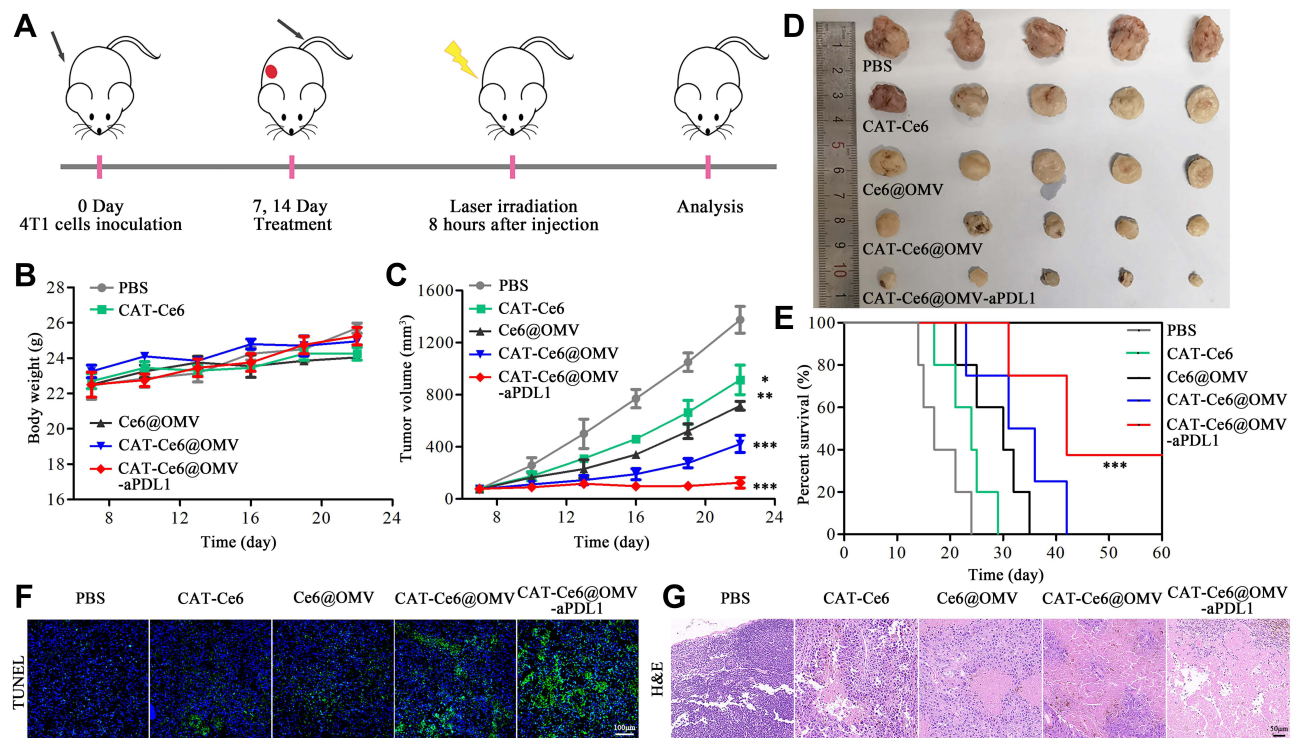
Figure 4 The anti-tumor effect of CAT-Ce6@OMV-aPDL1 under laser irradiation. (**A**) The diagrammatic sketch of CAT-Ce6@OMV-aPDL1 to suppress tumor growth in subcutaneous 4T1-tumor bearing model. The body weights (**B**) and tumor volumes (**C**) of the mice receiving different treatments. (**D**) Photographic images of tumors dissected from the mice receiving different treatments. (**E**) The survival rates of the mice receiving different treatments. TUNEL (**F**) and H&E (**G**) staining of tumor slices of mice receiving different treatments. Scale bar is 100 and 50 μm respectively. Data are presented as mean ± SD, statistical significance of (**C**) was analyzed by one-way ANOVA (compared with PBS group), and survival statistical significance was analyzed by log-rank (Mantel–Cox) test, *$P < 0.05$, **$P < 0.01$, ***$P < 0.001$.

and tumor volumes were measured every 3 days. As shown in Figure 4B, the body weights of five groups retained a steady rise throughout the treatment cycle, which represented rare side effects arising from different formulations. In comparison with uncontrolled tumor growth in PBS, CAT-Ce6 and Ce6@OMV groups, very significant tumor repression effects were observed in CAT-Ce6@OMV and CAT-Ce6@OMV-aPDL1 groups. The latter even caused tumor regression (Figure 4C and D). The survival curves of five groups confirmed the same results, representing improved anti-tumor effect of CAT-Ce6@OMV-aPDL1 (Figure 4E). After the last treatment, mice were dissected and tumor tissues were further analyzed by TUNEL and H&E staining. Stronger fluorescence signal of TUNEL was exhibited in CAT-Ce6 @OMV-aPDL1 group, authenticating a higher proportion of cell death, which was coincident with H&E staining (Figure 4F and G). These results demonstrated that the versatile strategy of CAT-Ce6@OMV-aPDL1 under laser irradiation would trigger tumor suppression to a large extent.

Activated Immune Responses After CAT-Ce6@OMV-aPDL1-Based PDT Treatment

After assessment of the anti-tumor effect of CAT-Ce6@OMV-aPDL1 under laser irradiation, we investigated the immune responses triggered by this strategy. Firstly, DCs activation was examined 5 days after the treatment cycle. FCM analysis showed that CAT-Ce6@OMV-aPDL1 enhanced the CD80, CD86 expression to a maximum extent, which represented significant enhanced DCs maturation. CAT-Ce6@OMV displayed a slightly worse effect, probably because CAT-Ce6@OMV-aPDL1 induced more tumor antigens generation from damaged tumor cells arising from the ICB treatment of aPD-L1 antibody (Figure 5A). These results validated that CAT-Ce6@OMV-aPDL1 coordination with laser irradiation could activate DCs pronouncedly. Similarly, tumor infiltration of CD8^{+} T cells was explored through CLSM. As shown in Figure 5B, two injections of CAT-Ce6@OMV-aPDL1 cooperating with laser irradiation increased tumor infiltration of CD8^{+} T cells obviously, testifying robust anti-tumor immune responses. Furthermore, given that many cytokines such as IFN-γ, TNF-α, IL-12p40 could initiate immune responses and inhibit tumor growth
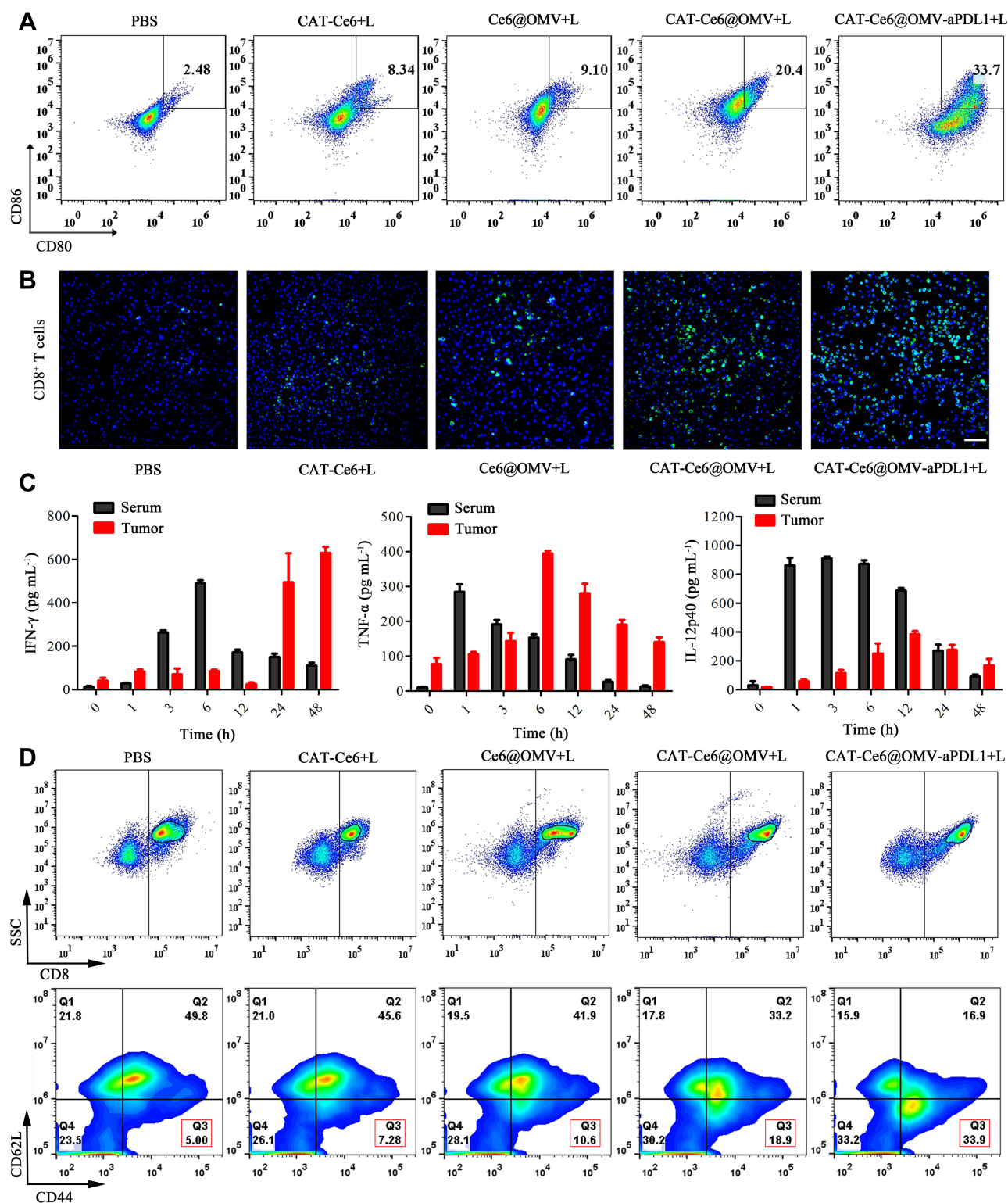
Figure 5 Investigation of immune responses in the 4T1-tumor bearing mice in vivo. (**A**) The percentage of mature DCs in the tumor tissues (gated on CD11c) 5 days after the last treatments. (**B**) The percentage of CD8$^+$ T cells infiltrated in the tumor tissues 5 days after the last treatments. (**C**) The concentration of cytokines in serum and tumor tissues after single injection of CAT-Ce6@OMV-aPDL1 to 4T1-tumor bearing mice at different time points (n = 3). (**D**) The percentage of effector memory CD8$^+$ T cells (CD44$^+$CD62L$^-$) in spleens 7 days after the last treatments.

and even metastasis,[34,46,47] we evaluated the concentrations of these cytokines in serum and tumor lysate after one intravenous injection of CAT-Ce6@OMV-aPDL1. In general, the concentrations of IFN-γ, TNF-α, IL-12p40 in serum increased rapidly at 1–6 h but tended to go back to base levels after 24 h, which suggested that CAT-Ce6@OMV-aPDL1 did not induce severe inflammatory responses and were well tolerated in mice. In contrast, the concentrations of cytokines in tumor lysate steadily increased as time went by and maintained middle level after 48 h, indicating a prolonged anti-tumor immune response (Figure 5C). In the end, we explored whether immune memory response was activated after the treatments. Seven days after the last treatment, spleen lysates were prepared for FCM analysis. It was found that CAT-Ce6@OMV-aPDL1 treatment produced more effector memory CD8$^+$ T cells (CD44$^+$CD62L$^-$), which may guarantee durable anti-tumor effect to prevent cancer recurrence and metastasis (Figure 5D). Collectively, these results illustrated that CAT-Ce6@OMV-aPDL1-based PDT induced more potent and longer anti-tumor immune responses without severe inflammatory responses, which was efficient for tumor therapy and practical for further applications.

Conclusion

In this work, we successfully fabricated a multifunctional nanosystem (CAT-Ce6@OMV-aPDL1) and wrapped CAT-Ce6 nanocomplex into aPDL1 modified OMVs (OMV-aPDL1), which solved the hydrophobicity problem of Ce6 without influencing the catalytic activity of catalase. On the one hand, this nanosystem not only mitigated the hypoxic feature of solid tumors, which was an inherent obstacle hindering the efficiency of PDT, but also relieved hypoxia for a long time in vivo. On the other hand, it activated anti-tumor immune responses, inducing more DCs and CD8$^+$ T cells migration to tumor tissues. Moreover, immune memory was found in the spleens of the mice receiving treatment twice. Ultimately, CAT-Ce6@OMV-aPDL1 suppressed tumor development remarkably, attributed to oxygenated PDT and immunotherapy. Therefore, this strategy incorporates oxygenated PDT, immunotherapy into a single, unified platform, which possesses huge potential for improving the efficiency of cancer treatment.

Acknowledgments

Disclosure

The authors report no conflicts of interest in this work.

References

1. Zou L, Wang H, He B, et al. Current approaches of photothermal therapy in treating cancer metastasis with nanotherapeutics. *Theranostics*. 2016;6 (6):762–772. doi:10.7150/thno.14988
2. Dolmans DEJGJ, Fukumura D, Jain RK. Photodynamic therapy for cancer. *Nat Rev Cancer*. 2003;3(5):380–387. doi:10.1038/nrc1071
3. Düzgüneş N, Piskorz J, Skupin-Mrugalska P, Goslinski T, Mielcarek J, Konopka K. Photodynamic therapy of cancer with liposomal photosensitizers. *Ther Deliv*. 2018;9(11):823–832. doi:10.4155/tde-2018-0050
4. Kwiatkowski S, Knap B, Przystupski D, et al. Photodynamic therapy – mechanisms, photosensitizers and combinations. *Biomed Pharmacother*. 2018;106:1098–1107. doi:10.1016/j.biopha.2018.07.049
5. Li M, Shao Y, Kim JH, et al. Unimolecular photodynamic O2-economizer to overcome hypoxia resistance in phototherapeutics. *ACS Appl Mater Interfaces*. 2020;142(11). doi:10.1021/jacs.0c00734
6. You Q, Zhang K, Liu J, et al. Persistent regulation of tumor hypoxia microenvironment via a bioinspired Pt-based oxygen nanogenerator for multimodal imaging-guided synergistic phototherapy. *Adv Sci*. 2020;7(17). doi:10.1002/advs.201903341
7. Damrongrungruang T, Kitchindaopat N, Thanasothon P, et al. Effects of photodynamic therapy with azulene on peripheral blood mononuclear cell viability and singlet oxygen formation. *Photodiagnosis Photodyn Ther*. 2018;24:318–323. doi:10.1016/j.pdpdt.2018.10.015
8. Chen H, Tian J, He W, Guo Z. H 2 O 2 -activatable and O 2 -evolving nanoparticles for highly efficient and selective photodynamic therapy against hypoxic tumor cells. *J Am Chem Soc*. 2015;137(4):1539–1547. doi:10.1021/ja511420n
9. Xu J, Xu L, Wang C, et al. Near-infrared-triggered photodynamic therapy with multitasking upconversion nanoparticles in combination with checkpoint blockade for immunotherapy of colorectal cancer. *ACS Nano*. 2017;11(5):4463–4474. doi:10.1021/acsnano.7b00715
10. Wan Y, Fu L, Li C, Lin J, Huang P. Conquering the hypoxia limitation for photodynamic therapy. *Adv Mater*. 2021;33(48):2103978. doi:10.1002/adma.202103978
11. Gunaydin G, Gedik ME, Ayan S. Photodynamic therapy—current limitations and novel approaches. *Front Chem*. 2021;9:691697. doi:10.3389/fchem.2021.691697

12. Ayan S, Gunaydin G, Yesilgul-Mehmetcik N, Gedik ME, Seven O, Akkaya EU. Proof-of-principle for two-stage photodynamic therapy: hypoxia triggered release of singlet oxygen. *Chem Commun*. 2020;56(94):14793–14796. doi:10.1039/D0CC06031C

13. Wang D, Wu H, Phua SZF, et al. Self-assembled single-atom nanozyme for enhanced photodynamic therapy treatment of tumor. *Nat Commun*. 2020;11(1):357. doi:10.1038/s41467-019-14199-7

14. Shen Z, Ma Q, Zhou X, et al. Strategies to improve photodynamic therapy efficacy by relieving the tumor hypoxia environment. *NPG Asia Mater*. 2021;13(1):39. doi:10.1038/s41427-021-00303-1

15. Phua SZF, Yang G, Lim WQ, et al. Catalase-integrated hyaluronic acid as nanocarriers for enhanced photodynamic therapy in solid tumor. *ACS Nano*. 2019;13(4):4742–4751. doi:10.1021/acsnano.9b01087

16. Cheng X, He L, Xu J, et al. Oxygen-producing catalase-based prodrug nanoparticles overcoming resistance in hypoxia-mediated chemo-photodynamic therapy. *Acta Biomater*. 2020;112:234–249. doi:10.1016/j.actbio.2020.05.035

17. Tu H, Sun H, Lin Y, et al. Oxidative stress upregulates PDCD4 expression in patients with gastric cancer via miR-21. *Curr Pharm Des*. 2014;20 (11):1917–1923. doi:10.2174/13816128113199990547

18. Tefik T, Kucukgergin C, Sanli O, Oktar T, Seckin S, Ozsoy C. Manganese superoxide dismutase Ile58Thr, catalase C-262T and myeloperoxidase G-463A gene polymorphisms in patients with prostate cancer: relation to advanced and metastatic disease. *BJU Int*. 2013;112(4):E406–E414. doi:10.1111/bju.12176

19. Huang Y, Fang W, Wang Y, Yang W, Xiong B. Transforming growth factor-β1 induces glutathione peroxidase-1 and protects from H 2O 2-induced cell death in colon cancer cells via the Smad2/ERK1/2/HIF-1α pathway. *Int J Mol Med*. 2012;29(5):906–912. doi:10.3892/ijmm.2012.901

20. Arnaut LG, Pereira MM, Dąbrowski JM, et al. Photodynamic therapy efficacy enhanced by dynamics: the role of charge transfer and photostability in the selection of photosensitizers. *Chem Eur J*. 2014;20(18):5346–5357. doi:10.1002/chem.201304202

21. Gündüz EÖ, Gedik ME, Günaydın G, Okutan E. Amphiphilic fullerene BODIPY photosensitizers for targeted photodynamic therapy. *Chem Med Chem*. 2021;17. doi:10.1002/cmdc.202100693

22. Jiang W, Tan Y, Yin JF, et al. Self-Assembly of amphiphilic BODIPY derivative and its nanoparticles as a photosensitizer for photodynamic therapy in corneal neovascularization. *Colloids Surf a Physicochem Eng Asp*. 2019;579:123706. doi:10.1016/j.colsurfa.2019.123706

23. Fan Z, Dai X, Lu Y, et al. Enhancing targeted tumor treatment by near IR light-activatable photodynamic-photothermal synergistic therapy. *Mol Pharm*. 2014;11(4):1109–1116. doi:10.1021/mp4002816

24. Cheng L, Gong H, Zhu W, et al. PEGylated Prussian blue nanocubes as a theranostic agent for simultaneous cancer imaging and photothermal therapy. *Biomaterials*. 2014;35(37):9844–9852. doi:10.1016/j.biomaterials.2014.09.004

25. Peng JR, Qi TT, Liao JF, et al. Mesoporous magnetic gold 'nanoclusters' as theranostic carrier for chemo-photothermal co-therapy of breast cancer. *Theranostics*. 2014;4(7):678–692. doi:10.7150/thno.7869

26. Fu X, Yang Z, Deng T, et al. A natural polysaccharide mediated MOF-based Ce6 delivery system with improved biological properties for photodynamic therapy. *J Mater Chem B*. 2020;8(7):1481–1488. doi:10.1039/c9tb02482d

27. Liu J, Han J, Kang Z, et al. In vivo near-infrared photothermal therapy and computed tomography imaging of cancer cells using novel tungsten-based theranostic probe. *Nanoscale*. 2014;6(11):5770–5776. doi:10.1039/c3nr06292a

28. Chatterjee DK, Fong LS, Zhang Y. Nanoparticles in photodynamic therapy: an emerging paradigm. *Adv Drug Deliv Rev*. 2008;60(15):1627–1637. doi:10.1016/j.addr.2008.08.003

29. Xia AL, Xu Y, Lu XJ. Cancer immunotherapy: challenges and clinical applications. *J Med Genet*. 2019;56(1):1–3. doi:10.1136/jmedgenet-2018-105852

30. Galluzzi L, Chan TA, Kroemer G, Wolchok JD, López-Soto A. The hallmarks of successful anticancer immunotherapy. *Sci Transl Med*. 2018;10:459. doi:10.1126/scitranslmed.aat7807

31. Yang Y. Cancer immunotherapy: harnessing the immune system to battle cancer. *J Clin Invest*. 2015;125(9):3335–3337. doi:10.1172/JCI83871

32. Zhai Y, He X, Li Y, et al. A splenic-targeted versatile antigen courier: iPSC wrapped in coalescent erythrocyte-liposome as tumor nanovaccine. *Sci Adv*. 2021;7(35):eabi6326. doi:10.1126/sciadv.abi6326

33. Riley RS, June CH, Langer R, Mitchell MJ. Delivery technologies for cancer immunotherapy. *Nat Rev Drug Discov*. 2019;18(3):175–196. doi:10.1038/s41573-018-0006-z

34. Gujrati V, Kim S, Kim SH, et al. Bioengineered bacterial outer membrane vesicles as cell-specific drug-delivery vehicles for cancer therapy. *ACS Nano*. 2014;8(2):1525–1537. doi:10.1021/nn405724x

35. Kim OY, Park HT, Dinh NTH, et al. Bacterial outer membrane vesicles suppress tumor by interferon-γ-mediated antitumor response. *Nat Commun*. 2017;8(1):1–9. doi:10.1038/s41467-017-00729-8

36. Kaparakis-Liaskos M, Ferrero RL. Immune modulation by bacterial outer membrane vesicles. *Nat Rev Immunol*. 2015;15(6):375–387. doi:10.1038/nri3837

37. Qing S, Lyu C, Zhu L, et al. Biomineralized bacterial outer membrane vesicles potentiate safe and efficient tumor microenvironment reprogramming for anticancer therapy. *Adv Mater*. 2020;32(47):2002085. doi:10.1002/adma.202002085

38. Gao J, Wang S, Dong X, Wang Z. RGD-expressed bacterial membrane-derived nanovesicles enhance cancer therapy via multiple tumorous targeting. *Theranostics*. 2021;11(7):3301–3316. doi:10.7150/THNO.51988

39. Constantinidou A, Alifieris C, Trafalis DT. Targeting programmed cell death −1 (PD-1) and ligand (PD-L1): a new era in cancer active immunotherapy. *Pharmacol Ther*. 2019;194:84–106. doi:10.1016/j.pharmthera.2018.09.008

40. Ribas A, Wolchok JD. Cancer immunotherapy using checkpoint blockade. *Science*. 2018;359(6382):1350–1355. doi:10.1126/science.aar4060

41. Qorraj M, Bruns H, Böttcher M, et al. The PD-1/PD-L1 axis contributes to immune metabolic dysfunctions of monocytes in chronic lymphocytic leukemia. *Leukemia*. 2017;31(2):470–478. doi:10.1038/leu.2016.214

42. Kim HS, Lee JH, Nam SJ, et al. Association of PD-L1 expression with tumor-infiltrating immune cells and mutation burden in high-grade neuroendocrine carcinoma of the lung. *J Thorac Oncol*. 2018;13(5):636–648. doi:10.1016/j.jtho.2018.01.008

43. Powles T, Eder JP, Fine GD, et al. MPDL3280A (anti-PD-L1) treatment leads to clinical activity in metastatic bladder cancer. *Nature*. 2014;515 (7528):558–562. doi:10.1038/nature13904

44. Xu T, Ma Y, Yuan Q, et al. Enhanced ferroptosis by oxygen-boosted phototherapy based on a 2-in-1 nanoplatform of ferrous hemoglobin for tumor synergistic therapy. *ACS Nano*. 2020;14(3):3414–3425. doi:10.1021/acsnano.9b09426

45. Liu C, Cao Y, Cheng Y, et al. An open source and reduce expenditure ROS generation strategy for chemodynamic/photodynamic synergistic therapy. *Nat Commun*. 2020;11(1):1735. doi:10.1038/s41467-020-15591-4

46. Kim OY, Park HT, Dinh NTH, et al. Bacterial outer membrane vesicles suppress tumor by interferon-γ-mediated antitumor response. *Nat Commun*. 2017;8(1):626. doi:10.1038/s41467-017-00729-8

47. Chen Q, Bai H, Wu W, et al. Bioengineering bacterial vesicle-coated polymeric nanomedicine for enhanced cancer immunotherapy and metastasis prevention. *Nano Lett*. 2020;20(1):11–21. doi:10.1021/acs.nanolett.9b02182